

# A First Look at Hydrogen Generation in an Ultramafic Rock with Micro-CT and SEM-BEX

Menke, Hannah P.<sup>1\*</sup>; Jangda, Zaid Z.<sup>2</sup>; Webb, Max<sup>1</sup>; Buckman, Jim<sup>1</sup>; Gough, Amy<sup>1</sup>

<sup>1</sup>Institute of GeoEnergy Engineering, Heriot-Watt University, Edinburgh, UK

<sup>2</sup>The Lyell Centre, Heriot-Watt University, Edinburgh, UK

## Key Points:

- We use 4D X ray micro-CT to image gas formation in a reacting ultramafic rock
- A gas phase appears during low temperature reaction of brine saturated ultramafic grains
- Electron microscopy shows mineral alteration and element redistribution consistent with fluid rock reaction
- Observations provide qualitative pore scale evidence relevant to natural hydrogen generation in the subsurface

arXiv:2512.09466v2 [cond-mat.other] 22 Dec 2025

---

Corresponding author: \*Hannah P. Menke, [h.menke@hw.ac.uk](mailto:h.menke@hw.ac.uk)

## Abstract

Natural hydrogen ( $H_2$ ) generated by water–rock interaction in ultramafic rocks is increasingly recognised as a potentially important primary energy resource, but the pore-scale processes that control the initiation and early transport of a free gas phase remain poorly constrained. Here we present an *in situ* X-ray micro-tomography experiment in which an ultramafic granular pack of ultramafic from Papua Province, Indonesia, saturated with KI-doped brine, is heated to  $100^\circ\text{C}$  with a pore pressure of 4 bar under 10 bar confining pressure inside a micro-CT scanner. Time-resolved 4D imaging captures the transition from a fully liquid-saturated pore space to the appearance and growth of a distinct gas phase after an  $\sim 8$  h induction period. Bubbles first nucleate near the top of the sample before becoming distributed throughout the imaged volume as a connected ganglia. The nucleating gas phase is most plausibly dominated by molecular hydrogen ( $H_2$ ) generated by low-temperature fluid–rock reaction, as indicated by independent hydrogen-presence detectors, although we cannot yet fully exclude minor contributions from other gases. SEM-BEX imaging reveals textural alteration and local changes in elemental signals between reacted and unreacted material. Taken together, these observations provide spatially and temporally resolved evidence for gas generation during low-temperature alteration of ultramafic grains and demonstrate that pore-scale imaging can directly link water–rock reaction kinetics, gas generation and multiphase flow behaviour in natural hydrogen systems.

## Plain Language Summary

Hydrogen gas can be produced naturally when certain ultramafic, iron-rich rocks formed in Earth’s mantle react with water. There is growing interest in whether this “natural hydrogen” could be used as a low-carbon energy source, but we still know very little about where the gas forms inside the rock and how it starts to move.

In this study, we packed grains of an ultramafic rock into a small cylinder, saturated them with salty water, and heated the system while it sat inside a 3D X-ray scanner (micro-CT). This let us watch the pore space inside the sample over time. At first, all of the pores contained only liquid. As the experiment continued, dark patches appeared and grew in the images, showing that a separate gas phase was forming. Two independent measurements of the gas produced during the experiment are consistent with hydrogen, although this single experiment cannot fully describe all of the reactions taking place.

After imaging, we examined the reacted grains under an electron microscope and saw evidence that the minerals had altered and some elements had moved. Together, these observations demonstrate that we can directly visualise gas generation inside reactive rocks at relatively low temperatures. This is an early, exploratory step towards understanding how natural hydrogen might form and behave in the subsurface.

## 1 Introduction

Natural geologic hydrogen ( $H_2$ ) is emerging as a potentially vast, carbon-free primary energy resource that could complement, or in some settings substitute, engineered “green”  $H_2$  production. Global compilations of gas analyses from seeps, boreholes and mines show that  $H_2$  is far more widespread than previously appreciated and occurs in many tectonic settings, often as a major component of the gas phase (Zgonnik, 2020). Recent system-scale syntheses formalise the concept of a “ $H_2$  system”, in which  $H_2$  is generated, migrates and accumulates in traps in an analogous way to hydrocarbons (Jackson et al., 2024; Prinzhofer & Deville, 2015), and multi-scale reviews highlight the key migration pathways and timescales from the planetary to basin scale (Lodhia et al., 2024). This has led to growing industrial interest in “native” or “natural” hydrogen, with first-

order assessments suggesting that alteration-driven systems (e.g. areas of serpentinisation) could sustain commercially significant fluxes over geological timescales (Gaucher, 2020), and to proposals for engineered “rock-based” hydrogen concepts (white and “orange” hydrogen) that explicitly exploit water–rock reactions in mafic and ultramafic rocks as part of the low-carbon hydrogen portfolio (Osselin et al., 2022).

Among the diverse proposed sources of natural H<sub>2</sub>, low- to high-temperature serpentinization of ultramafic rocks is generally considered the most efficient and volumetrically important (Oze & Sharma, 2007; McCollom & Bach, 2009; Jackson et al., 2024). In this process, Fe<sup>2+</sup>-bearing primary minerals such as olivine and pyroxene react with water to form Fe<sup>3+</sup>-bearing phases (e.g., magnetite, Fe(III)-serpentine), generating H<sub>2</sub> as a by-product (Sleep et al., 2004; Holm et al., 2015). Thermodynamic and kinetic models predict that H<sub>2</sub> yields depend sensitively on temperature, water-to-rock ratio, mineralogy, water chemistry, and redox state (McCollom & Bach, 2009; McCollom et al., 2016; Ely et al., 2023), while field observations from ophiolites and oceanic and continental settings (e.g., Samail ophiolite, Oman; Lost City hydrothermal field) demonstrate that serpentinization can sustain long-lived fluxes of H<sub>2</sub>-rich, hyperalkaline fluids (Schrenk et al., 2013). More recently, work in the Samail ophiolite Oman has shown that significant H<sub>2</sub> can also be generated during late, low-temperature (< 200°C) alteration of already serpentinized peridotite, extending the window of H<sub>2</sub> production to cooler, near-surface conditions (Ellison et al., 2021).

Experimental studies have been crucial in constraining the rates and controls of H<sub>2</sub> generation, but they are dominated by batch or flow-through reactor experiments containing powders or finely crushed rock. Low-temperature (30–150°C) experiments on partially serpentinized peridotite and olivine powders show H<sub>2</sub> production over days to months, with rates and yields strongly influenced by grain size, the presence of magnetite and fluid composition (Mayhew et al., 2013; Miller et al., 2016; Neubeck et al., 2014; McCollom et al., 2016). More recently, flow-through experiments on olivine under hydrothermal conditions have demonstrated sustained H<sub>2</sub> generation under continuous fluid circulation and further quantified the coupling between serpentinization, reaction progress and H<sub>2</sub> release (Ross et al., 2025). These studies underpin current parameterisations of H<sub>2</sub> generation in natural systems and highlight the importance of reactive Fe-bearing phases, brucite stability and feedbacks between pH, carbonate activity and secondary mineral precipitation (Schrenk et al., 2013). However, because powders maximise reactive surface area and eliminate a connected pore space, they provide little insight into where in a consolidated rock H<sub>2</sub> actually nucleates, how rapidly it forms a separate gas phase, or how pore-scale connectivity and mineral heterogeneity control the transition from dissolved to free gas.

Core-scale reactive transport experiments bridge part of this gap by preserving rock fabric and permeability while allowing continuous geochemical monitoring. Percolation of reactive fluids through ultramafic rocks and serpentinites has demonstrated strong couplings between serpentinization, carbonation, permeability reduction and H<sub>2</sub> production (e.g., Wang et al., 2019; Albers et al., 2021; Farough et al., 2016). Yet in most such studies the rock behaves as a “black box”: H<sub>2</sub> production is inferred from outlet fluid chemistry or headspace analyses, and any gas phase that forms inside the pore network remains invisible. Even in well-characterised natural systems such as the Samail ophiolite, constraints on H<sub>2</sub> generation and transport rely primarily on fluid chemistry, isotopes and mineralogical proxies rather than direct imaging of the gas phase itself (Miller et al., 2016; Ellison et al., 2021). As a result, the fundamental pore-scale mechanisms governing the *initiation* and early *transport* of H<sub>2</sub>, bubble nucleation sites, snap-off events, critical gas saturation and connectivity, are still poorly constrained.

In parallel, a large and rapidly growing body of work has used X-ray micro-tomography (micro-CT) to image dynamic multiphase flow and reactive transport in rocks. Time-resolved (4D) micro-CT has been applied to dissolution and precipitation in carbonates

and sandstones, enabling direct observations of evolving pore structures, wormholing and reaction-front dynamics under reservoir conditions (Noiriel & Soulaine, 2021; Noiriel & Renard, 2022; Menke et al., 2015). Similar techniques have been used to quantify residual trapping and ganglion dynamics during CO<sub>2</sub>-brine flow, to measure capillary pressure-saturation relationships, and to calibrate pore-network and direct numerical simulations (Andrew et al., 2014; Jiang & Tsuji, 2015; Bultreys et al., 2016). These studies demonstrate that 4D imaging can resolve micron-scale fluid-fluid and fluid-solid interfaces, capturing non-linear displacement patterns, snap-off and reconnection events that strongly influence macroscopic transport properties.

Only recently has this pore-scale imaging toolkit been applied to H<sub>2</sub> itself. Micro-CT studies of H<sub>2</sub>-brine flow in sandstones show that H<sub>2</sub> behaves as a non-wetting phase in many reservoir-relevant conditions, with significant capillary trapping, strong sensitivity to rock heterogeneity and subtle but important differences from CO<sub>2</sub>-brine systems (Thaysen et al., 2023; Jangda et al., 2023; Rezaei et al., 2022). These works provide critical benchmarks for underground H<sub>2</sub> storage, but they all consider externally injected H<sub>2</sub> displacing brine; the H<sub>2</sub> is not generated *in situ* by water-rock reaction. Complementary core-flooding experiments and relative permeability measurements reveal that H<sub>2</sub>-water flow in rocks is typically capillary-limited, with low minimum water saturations and relative permeability curves that differ from those of CO<sub>2</sub>-water systems (Yekta et al., 2018; Rezaei et al., 2022; Boon & Hajibeygi, 2022). Reviews of underground H<sub>2</sub> storage emphasise that uncertainties in pore-scale trapping, dissolution and reaction with the rock and microbiota are among the key scientific challenges for safe and efficient large-scale deployment (Heinemann et al., 2021; Miocic et al., 2023).

Despite these advances, a critical observational gap remains at the intersection of serpentinization geochemistry and pore-scale multiphase flow physics. To our knowledge, there are no prior studies that directly image the nucleation and growth of an H<sub>2</sub> gas phase *as it is produced* within an ultramafic rock under hydrothermal conditions. Existing serpentinization experiments constrain bulk H<sub>2</sub> generation rates but lack spatially resolved information on gas formation, while pore-scale H<sub>2</sub> imaging studies focus on storage scenarios with externally supplied gas. This missing link limits our ability to assess whether H<sub>2</sub> generated during low-temperature alteration can reach saturations and connectivity sufficient for migration and accumulation, or whether it is predominantly trapped and dissolved within low-permeability alteration halos.

In this study, we address this gap using a proof-of-concept *in situ* experiment that combines time-resolved 4D micro-CT imaging with post-mortem SEM and BEX analyses of an ultramafic granular pack reacting with brine at 100°C and 4 bar pore pressure. Our approach allows us to (i) document the transition from a fully liquid-saturated pore network to the appearance and subsequent growth of a distinct gas phase, (ii) qualitatively characterise the spatio-temporal patterns of bubble nucleation and coalescence within the rock framework, and (iii) relate these physical observations to textural and compositional changes observed in SEM-BEX images, including the development of secondary phases and local variations in elemental signals. When considered together with independent measurements of gas generation, these observations are consistent with low-temperature H<sub>2</sub> production via water-rock reaction, but they do not on their own uniquely fully resolve the reaction pathways. We therefore present this single, exploratory experiment as an initial step towards linking serpentinization-driven gas generation with pore-scale transport physics in natural H<sub>2</sub> systems, and we explicitly highlight the limitations and uncertainties that future, more targeted studies will need to address.

## 2 Materials and Methods

### 2.1 Sample Selection and Preparation

The experiment utilized an ultramafic rock sample selected for its potential for low-temperature serpentinization. The sample was collected from the mantle sequence of the Cyclops Ophiolite located in the Cyclops Mountains of Papua Province, Indonesia (along the northern coast of the island of New Guinea). Petrographic inspection shows extensive alteration consistent with serpentinization, with relict olivine grains preserved within a fine-grained alteration matrix.

The rock was crushed and dry sieved to isolate the coarse fraction, retaining only grains between 0.6-1 mm. This grain size was selected to ensure a resolvable pore network for 3D imaging while maintaining reactive surface area.

### 2.2 Experimental Setup and Protocol

All experiments were conducted at a temperature of 100°C. The pore space was saturated with KI-doped brine at a pore pressure of 4 bar, while the core holder was loaded within a Hassler-type sleeve under an external confining pressure of 10 bar. Unless otherwise stated, pressures quoted in this study refer to pore pressure. At the experimental temperature of 100°C and a pore pressure of 4 bar, the KI-doped brine is well below its saturation vapour pressure (water boils at 100°C only at  $\sim 1$  bar), although a small amount of water vapour will always be present in any gas phase in equilibrium with liquid water. We therefore do not expect boiling or a persistent steam phase under these conditions; any free gas that appears must arise from exsolution of non-condensable species rather than liquid water boiling.

The granular sample was loaded into a custom-built X-ray transparent core holder designed for high-pressure and high-temperature flow experiments. A strip of H<sub>2</sub> indicator was attached inside the confining sleeve of the core holder to detect the presence of H<sub>2</sub>. The rig was mounted within the X-ray micro-tomography (micro-CT) scanner to facilitate *in situ* imaging (Fig. 1).

The initial saturation protocol was designed to eliminate trapped air and ensure full liquid saturation prior to heating. First, the sample was flushed with CO<sub>2</sub> at ambient conditions. The system was then confined at 10 bar pressure. Subsequently, the sample was flooded with a brine solution composed of 5 wt% potassium iodide (KI) at a pore pressure of 4 bar to keep the brine in the liquid phase. KI was used as an X-ray contrast agent to enhance the attenuation of the fluid phase, thereby maximizing the contrast between the rock grains (grey), the brine (bright white), and any generated gas (black). At this concentration KI is not expected to strongly modify the low-temperature alteration reactions compared to chloride brines, and we did not observe any textural or compositional evidence for abundant KI salt precipitates in the post-reaction samples. The system was flooded for 1000 Pore Volumes (PV) to ensure the complete dissolution of the initial CO<sub>2</sub> into the brine, ensuring that any gas phase observed later resulted from reaction rather than trapped shielding gas.

Following the brine saturation phase, flow was halted (static conditions with no net through-flow), and the temperature of the sample was raised to 100°C to initiate the hydrothermal reaction. During this static stage, pore pressure is maintained at 4 bar, so any volumetric expansion associated with gas exsolution was accommodated by small displacements of brine into the pump rather than by a significant increase in pore pressure.

Following the conclusion of the *in situ* experiment, the system was degassed and the H<sub>2</sub> concentration in the pump gas effluent was monitored using a portable electrochemical H<sub>2</sub> detector (RAE ToxiRAE Pro PGM-1860). This instrument provides pres-

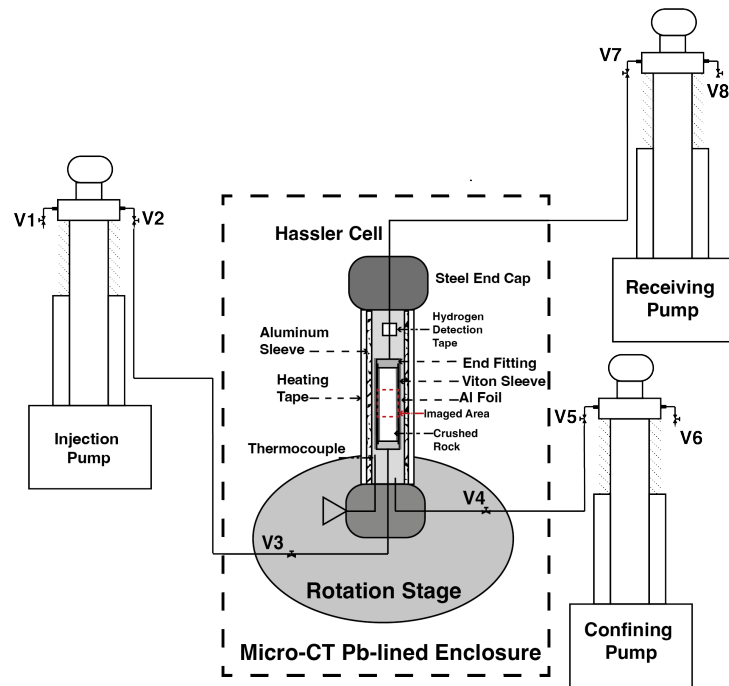


**Figure 1.** Experimental set-up for in situ micro-CT imaging of H<sub>2</sub> generation and gas exsolution. A Hassler-type core holder containing crushed ultramafic rock is mounted on the rotation stage inside a Pb-lined micro-CT enclosure. The sample is confined by a Viton sleeve and aluminium foil within an aluminium outer sleeve, with steel end caps and end fittings connecting to the flow lines. Heating tape and a thermocouple control and monitor the sample temperature, and H<sub>2</sub>-indicator tape is placed around the core to detect any leakage. Pore fluid is injected from the injection pump, while the receiving pump maintains pressure and collects effluent. Confining pressure is applied via the confining pump. The red dashed box indicates the imaged region within the core.

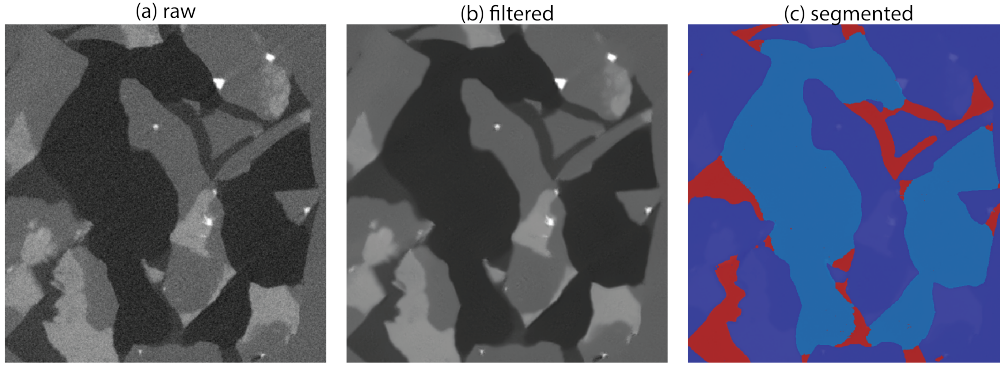


**Figure 2.** Representative 2D slice showing the micro-CT image processing workflow. (a) Raw greyscale image, (b) the same slice after non-local means filtering to reduce high-frequency noise while preserving phase boundaries, and (c) final three-phase segmentation into solid grains (dark blue), brine-filled pore space (red) and gas voxels (light blue).

ence/threshold measurements of  $H_2$  in the ppm range rather than a full gas composition, but it allows us to confirm whether  $H_2$  is present above background levels during controlled depressurisation. The reacted sample was then removed from the core holder and the  $H_2$ -indicator strip was retrieved from the confining sleeve.

### 2.3 Micro-CT Image Acquisition

Time-resolved 3D images were acquired during the heating phase at a spatial resolution of  $6.277 \mu\text{m}$ . This resolution is sufficient to capture inter-granular porosity and gas bubble nucleation events. During the first 8 hours the images were taken every 50 mins with no  $H_2$  detected until scan 11. After the onset of gas formation had been captured, the imaging interval was increased and the sample was imaged again only at 23 and 30 hours. Each 3D image took approximately 50 mins to acquire with 800 projections at 100 KeV and 9.9 Watts and 2 frames/s in an Rx EasyTom micro-CT scanner.

### 2.4 Micro-CT Image Analysis

To quantify the evolution of the gas phase, all time-lapse micro-CT volumes were processed using a consistent image-analysis workflow in the image processing software Avizo 2025.1 (Thermo Fisher Scientific). First, each scan was rigidly registered to the initial reference scan by maximising mutual information between grey-scale volumes and resampled onto the reference grid using a Lanczos kernel (Lanczos, 1956) to preserve edge sharpness. Second, we applied a non-local means filter to reduce high-frequency noise while retaining phase boundaries in the greyscale images (Buades et al., 2005). Third, the solid, brine and gas phases were segmented in the Avizo Segmentation Editor using simple global grey-level thresholding, guided by the histogram and visual inspection of representative slices. Conservative thresholds were chosen to separate solid from pore space, and within the pore space voxels with the lowest attenuation were classified as gas. Small isolated gas clusters below a few voxels were removed as likely noise using basic morphological operations. A representative 2D slice illustrating the raw, filtered and segmented images is shown in Figure 2. For each time step we then calculated bulk gas saturation as the ratio of gas-filled voxels to pore-space voxels. Visual inspection of representative slices and 3D renderings was used to check the segmentation quality; we therefore regard the resulting saturation values as approximate but internally consistent across the time series.

To check that our conclusions do not depend on a single arbitrary choice of thresholds, we also inspected segmentations generated using slightly more and less conservative gas–brine thresholds that were still consistent with the grey-level histograms and visual appearance of the images. These alternative segmentations yielded very similar temporal trends in bulk  $S_g$  and connectivity, and in particular preserved the three-stage evolution (no resolvable gas, rapid increase, slower late-time growth).

Gas ganglia statistics were obtained from the segmented gas phase using Avizo’s *Label Analysis* module. Connected-component labelling was applied to the binary gas mask to identify individual gas clusters (ganglia), and for each cluster we extracted its volume. From these we computed the distribution of ganglia sizes, the number density of clusters, and the volume fraction of the largest cluster  $f_{\max}$  at each time step.

Percolation behaviour was assessed by checking whether the largest cluster formed a continuous path spanning the sample between opposing faces (top–bottom and/or side–side) based on voxel-wise connectivity. In other words, a cluster was classified as percolating if it provided a continuous, spanning pathway through the imaged volume; large, internally connected ganglia that did not satisfy this spanning criterion were treated as non-percolating.

## 2.5 SEM and BEX analysis

Pre- and post-reaction grains for electron microscopy were prepared from the same bulk material as the micro-CT sample. Sub-samples were gently dry-sieved to remove dust, sprinkled onto aluminium stubs, and immobilised using conductive adhesive carbon tabs (Agar Scientific). No specific rinsing step was applied to remove KI brine residues prior to drying, so we cannot completely exclude the possibility that a minor fraction of the observed surface features reflects salt precipitation upon drying. However, the platy surface crystals and roughened patches we focus on occur in discrete areas whose BEX signatures are dominated by Mg, Al, Ca and Fe rather than K or I (Table 2), and their morphology differs from simple euhedral halide crystals. We therefore interpret them primarily as alteration-related features rather than dried KI.

The mounts were imaged using an FEI Quanta FEG 650 Scanning Electron Microscope (SEM) operated in low-vacuum mode. Backscattered electron (BSE) images were acquired at magnifications of hundreds to several thousand times to capture both grain-scale morphology and fine-scale surface textures. For each mount, we collected combined backscatter and energy-dispersive X-ray (BEX) data using an Oxford Instruments Unity detector in combination with an X-Max<sub>N</sub> 150 mm Energy Dispersive X-ray (EDX) detector. These generate colour-composite elemental maps by assigning selected element signals (e.g., Mg, Al, Si, Ca, Fe) to different colour channels along with quantitative elemental analysis. These BEX composites were used to visualise spatial variations in surface composition across many grains using the Oxford Instruments AZtec 6.2™ software. In addition, five spot elemental analyses were acquired on each mount, targeting representative areas on the larger grains, and the resulting ranges in composition are reported in Table 2. No matrix-specific corrections were applied beyond the standard instrument routines, so the spot analyses are interpreted qualitatively and in conjunction with the textural information from the BSE and BEX images.

## 3 Results

### 3.1 In situ observation of H<sub>2</sub> nucleation and growth

The 4D micro-CT scans provided a direct visualization of gas phase evolution within the pore space. During the initial heating and early static reaction period, the pore space remained fully brine-saturated (Figure 3a), with an image-derived porosity of  $\phi = 0.375$

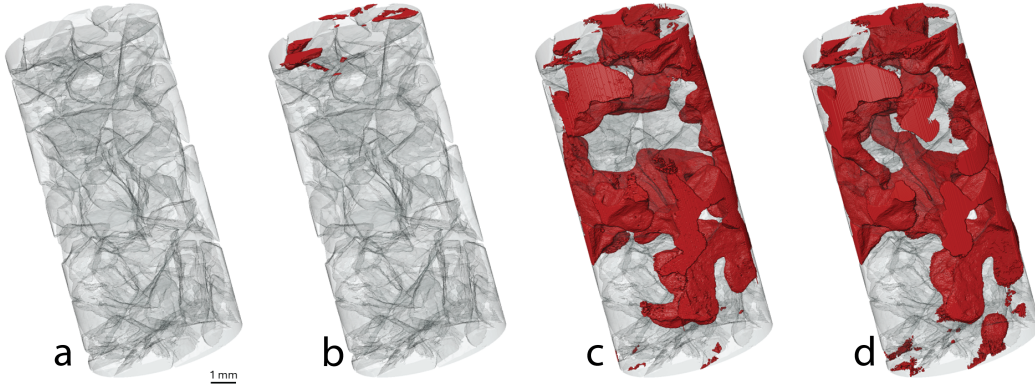


**Figure 3.** Time series of segmented gas phase (false-colour red) within the ultramafic granular pack at (a) 0, (b) 8, (c) 23, and (d) 30 hours. The grains are rendered as translucent grey and the brine is transparent, so that the red overlay highlights only the voxels classified as gas in the micro-CT segmentation.

and a specific solid–pore interfacial area of  $A/V_s = 1.13 \times 10^4 \text{ m}^2 \text{ m}^{-3}$  (Table 1a). No gas voxels were detected at this stage ( $S_g = 0$ ).

Gas bubble nucleation was first observed at 8 hours, when a small number of discrete bubbles appeared, localised primarily at the top of the sample column (Figure 3b). At this time the bulk gas saturation remained very low ( $S_g \approx 0.01$ ; Table 1b), indicating that only a tiny fraction of the pore space had exsolved. Importantly, the experiment had already been at (approximately) constant temperature and pore pressure for several hours by this point, so this delayed onset is difficult to reconcile with simple thermal expansion of trapped air or immediate exsolution of pre-existing dissolved gas during the initial heating ramp. Instead, it is more naturally interpreted as the time required to generate and accumulate reaction-derived  $\text{H}_2$  to supersaturation.

By the subsequent scan at 23 hours, bubble nucleation and growth had propagated throughout the imaged volume (Figure 3c). The bulk gas saturation had increased to  $S_g \approx 0.39$ , corresponding to an average rate of change  $\Delta S_g / \Delta t \approx 2.6 \times 10^{-2} \text{ h}^{-1}$  between 8 and 23 hours (Table 1b; Figure 5). This period therefore marks a rapid onset of widespread supersaturation and gas generation within the pore space. Continued observation at 30 hours showed a further but more modest increase in bulk gas saturation to  $S_g \approx 0.43$ , with a much lower apparent rate of change ( $\Delta S_g / \Delta t \approx 5.9 \times 10^{-3} \text{ h}^{-1}$ ) over the final 7 hours (Figure 3d; Table 1b; Figure 5). Visually, bubbles increased slightly in size and began to coalesce, suggesting a transition from predominantly nucleation-driven growth to a regime dominated by diffusive growth and coalescence.

Vertical profiles of gas saturation  $S_g(z)$  along the core axis (Figure 4) further illustrate this evolution. At 8 h the gas phase is confined to a thin zone near the top of the imaged interval, with  $S_g$  close to zero over most of the depth range. By 23 h, gas saturations of  $\sim 0.3$ – $0.8$  extend through much of the interior of the sample, while only the basal few hundred micrometres remain largely brine saturated. The profiles retain a clear top bias, as expected for a low-density gas such as  $\text{H}_2$ , but significant gas fractions are also present at depth, implying that capillary forces and local pore geometry are sufficient to trap and hold ganglia against buoyancy once nucleation has occurred. The profile at 30 h has a similar overall shape but slightly higher  $S_g$  in parts of the column, con-

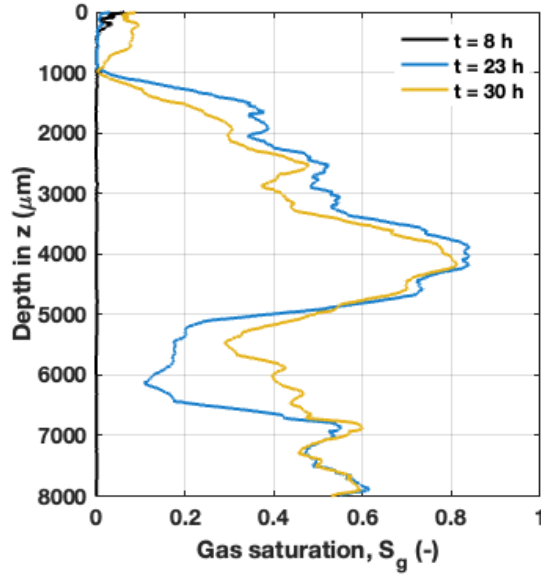


**Figure 4.** Vertical profiles of gas saturation  $S_g$  as a function of depth  $z$  along the core axis at 8, 23 and 30 h. Depth increases downward from the top of the imaged sample and is expressed in micrometres; line colours correspond to the times indicated in the legend.

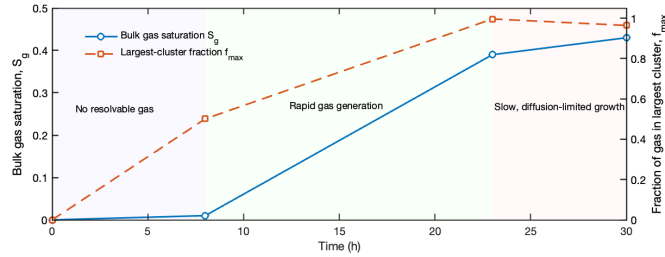


**Figure 5.** Evolution of bulk gas saturation  $S_g$  (left axis, solid blue line) and the fraction of gas in the largest cluster  $f_{\max}$  (right axis, dashed orange line) as a function of time during the experiment. Shaded bands indicate the three stages inferred from the image-derived metrics: (i) no resolvable gas (0–8 h), (ii) rapid gas generation and connectivity growth (8–23 h), and (iii) slower, diffusion-limited growth (23–30 h).

sistent with modest late-time growth and coalescence of existing ganglia rather than widespread nucleation of new bubbles.

Overall, the time-lapse imaging and derived metrics support a three-stage evolution (Figures 3 and 5; Table 1b): (i) an initial fully saturated stage with no detectable gas (0–8 h), (ii) a rapid gas generation stage with strongly increasing  $S_g$  (8–23 h), and (iii) a slower growth stage in which  $S_g$  approaches an apparent plateau (23–30 h). Quantitative connectivity metrics (cluster statistics and percolation, including  $f_{\max}$ ; Figure 5; Table 1b) further characterise changes in gas ganglia structure and will be discussed in Section 4.

**Table 1.** Summary of image-derived metrics used in the kinetic and connectivity analysis.  $\phi$  is porosity,  $A$  the solid–pore interfacial area within the imaged volume,  $S_g$  the bulk gas saturation,  $\Delta S_g/\Delta t$  the approximate rate of change between scans, and  $f_{\max}$  the volume fraction of the largest gas cluster relative to total gas volume.

<i>(a) Static micro-CT geometry at <math>t = 0</math>.</i>						
	$t$	$\phi$	$A/V_s$	$A$		
	(h)	(-)	( $\text{m}^2 \text{m}^{-3}$ )	( $\text{m}^2$ )		
	0	0.375	$1.13 \times 10^4$	$4.27 \times 10^{-4}$		
<i>(b) Time-lapse gas saturation and connectivity metrics.</i>						
Scan	$t$	$S_g$	$\Delta t$	$\Delta S_g/\Delta t$	$f_{\max}$	Perc.
	(h)	(-)	(h)	( $\text{h}^{-1}$ )	(-)	(Yes/No)
1	0	0.00	–	–	0	No
2	8	0.01	8	$8.74 \times 10^{-4}$	0.501	No
3	23	0.39	15	$2.56 \times 10^{-2}$	0.996	No
4	30	0.43	7	$5.87 \times 10^{-3}$	0.964	No <sup>†</sup>

<sup>†</sup>Largest cluster touches both the top and bottom boundaries of the imaged volume but does not form a fully continuous spanning path at the voxel scale.

Given the pre-removal of  $\text{CO}_2$  via the extensive 1000 PV brine flush, the absence of any intentionally introduced gas phase, and the fact that water remains well below its boiling point at  $100^\circ\text{C}$  and 4 bar, the nucleating gas is most plausibly dominated by molecular  $\text{H}_2$  generated via hydrothermal alteration of the ultramafic grains. The high-contrast KI brine allows the gas phase to be segmented unambiguously against the rock matrix in the micro-CT images. Independent presence indicators further support this interpretation: during controlled depressurisation at the end of the experiment the electrochemical detector registered  $\text{H}_2$  concentrations up to  $\sim 80$  ppm in the pump gas effluent, and the  $\text{H}_2$ -indicator strip in the confining sleeve showed a positive response. However, these measurements provide presence/threshold information rather than a full gas composition, so minor contributions from other volatiles (e.g., residual dissolved gases or water vapour) cannot be completely ruled out.

### 3.2 Mineralogical Alteration and Geochemistry

BEX composite images of the grain mounts show that both the pre- and post-reaction samples are compositionally heterogeneous at the grain scale, but the distribution and intensity of the colour-coded elemental response change after reaction (Fig. 6a,e). In the reacted sample, patches of higher intensity occur on a subset of grains in both the multi-element composite and the Fe-only maps (Fig. 6b,f), indicating localised changes in surface composition rather than a uniform alteration of all grains.

Post-experiment SEM imaging revealed distinct, localised textural changes compared to the unreacted control (Fig. 6c,d,g,h). In the pre-reaction sample, grain surfaces at the overview scale are relatively smooth and, at higher magnification, consist mainly of compact, equant to sub-rounded microcrystalline material with no obvious oriented growths (Fig. 6c,d). In contrast, the reacted grains show more irregular, roughened surfaces and, in places, clusters of elongate to platy crystals protruding from the grain surface into the pore space (Fig. 6g,h). These features occur in discrete patches rather than covering entire grains, and we interpret them as localised secondary alteration products.

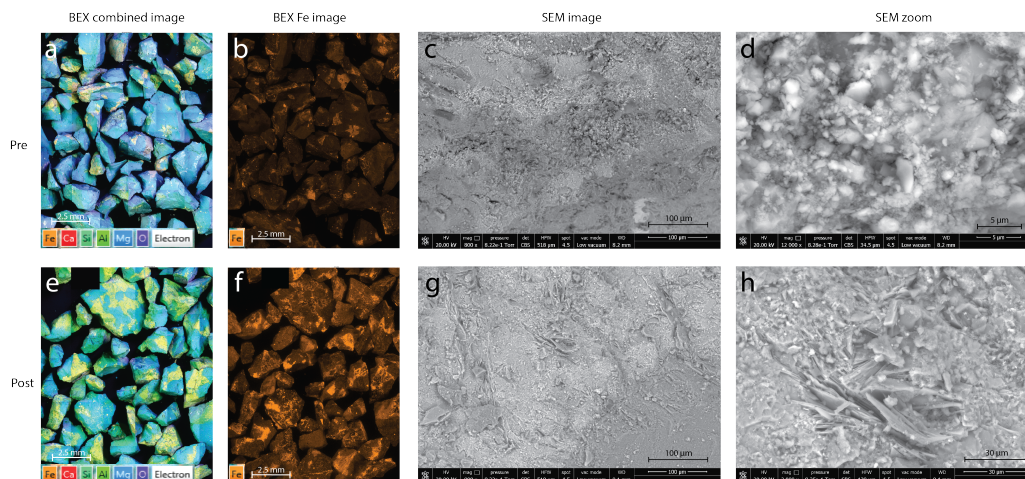


**Figure 6.** Representative BEX and SEM images of the ultramafic grains before and after reaction. (a,e) Multi-element BEX composite images of pre- and post-reaction mounts showing compositionally heterogeneous but broadly Mg-rich grains, with locally enhanced signals after reaction. (b,f) Fe-only BEX maps highlighting Fe-enriched patches on a subset of grains. (c,g) SEM overview images of pre- and post-reaction grain surfaces. (d,h) Higher-magnification SEM zooms illustrating the transition from relatively smooth, compact pre-reaction surfaces (d) to roughened surfaces with discrete clusters of elongate to platy surface crystals protruding into the pore space in the reacted sample (h). These features are interpreted as localised secondary alteration products and compositional reorganisation at grain surfaces.

BEX spot analyses highlight corresponding local variations in elemental signals between the pre- and post-reaction grains (Table 2). Across the five pre-reaction spots, Mg- and Fe-rich compositions dominate and Al and Ca remain relatively low, whereas the post-reaction spots show a broader spread with locally elevated Al and Ca and Mg (and, to a lesser extent, Fe) extending to lower values. One plausible explanation is partial dissolution of Mg-rich primary phases, leaving behind or exposing domains that are comparatively enriched in Al and associated Ca-bearing material, possibly including thin secondary coatings where the elongate crystals are observed. We cannot completely exclude a contribution from salt precipitation upon drying, given the presence of KI in the brine, but in the areas analysed the BEX signals are dominated by Mg, Al, Ca and Fe and do not show elevated K or I consistent with pure KI crystals. Similar Al- and Ca-enriched alteration products have been reported in low-temperature alteration of ultramafic rocks and are commonly attributed to Al-bearing phyllosilicates or related secondary phases. However, the BEX data are semi-quantitative and each spot samples only a very small area; the observed ranges may therefore reflect a combination of reaction-driven changes and pre-existing micro-scale heterogeneity. We consequently treat the elevated Al and Ca signals as qualitative indicators of local mineralogical reorganisation at grain surfaces rather than as evidence for bulk-scale Al mobilisation or the formation of specific, well-identified Al-bearing mineral phases.

Taken together, the SEM-BEX observations are consistent with ongoing fluid–rock reaction in the vicinity of the pore space during the experiment, leading to modification of grain surfaces. A more complete characterisation of the alteration products and their compositions would require targeted phase identification (e.g., diffraction or spectroscopy) and more extensive microanalytical sampling, which are beyond the scope of this proof-of-concept study.

**Table 2.** Elemental composition from bulk XRF and BEX spot analyses before (pre) and after (post) reaction. BEX values give the minimum–maximum range of wt. % across five spot analyses on each mount. Dashes indicate elements not detected in any of the BEX spots.

Element	Bulk XRF	BEX pre	BEX post
	wt. %	wt. % (range)	wt. % (range)
O	–	48.10–51.92	49.48–51.58
C	–	5.09–6.64	–
Na	0.045	–	–
Mg	20.127	18.88–20.97	14.44–21.10
Al	2.213	1.44–2.50	3.09–6.58
Si	17.524	16.38–18.97	15.19–17.49
P	0.018	–	–
S	0.008	–	–
K	0.003	–	0.23–0.23
Ca	1.780	0.36–0.36	0.26–6.11
Ti	0.081	0.06–0.06	–
Mn	0.108	0.13–1.22	0.34–0.34
Fe	6.542	5.32–6.80	5.19–7.29
Ni	0.156	0.17–0.42	0.20–0.20
Cr	0.691	0.11–0.30	0.40–0.40
Sr	0.001	–	–
Zn	0.018	–	–
Ba	0.009	–	–
Zr	0.006	–	–
Yb	–	–	0.90–0.90

## 4 Discussion

The time series of pore-scale images and derived metrics shows three distinct regimes (Figures 3 and 5; Table 1): (i) an initial period with no resolvable gas phase (0–8 h), (ii) a rapid transition to a connected network of bubbles between 8 and 23 h, and (iii) a subsequent phase of more modest bubble growth between 23 and 30 h. Although our experiment was not designed for precise kinetic inversion, simple order-of-magnitude estimates, constrained by the image-derived porosity, surface area and gas saturations, help to show that these regimes are consistent with delayed supersaturation, nucleation and subsequent diffusion-limited growth of an H<sub>2</sub> gas phase.

The delay before the first visible bubbles can be understood as the time needed to build up a sufficient concentration of dissolved H<sub>2</sub> in the pore water. From the micro-CT field of view and core-holder geometry, the total sample volume is of order  $V_s \sim 10^{-7} \text{ m}^3$ , and the segmented images give a porosity of  $\phi = 0.375$ , so that the pore volume is  $V_p \approx \phi V_s \approx 4 \times 10^{-8} \text{ m}^3$  ( $\sim 0.04 \text{ mL}$ ). Published measurements and correlations for H<sub>2</sub> solubility in pure water and NaCl brines at temperatures near 100°C and H<sub>2</sub> partial pressures of order 1–10 bar give equilibrium dissolved concentrations of  $c_{\text{sat}} \approx (2\text{--}6) \times 10^{-4} \text{ mol L}^{-1}$  (e.g., Wiesenburg & Guinasso Jr, 1979). At these conditions the pore fluid remains entirely in the liquid phase (water vapour pressure at 100°C is  $\sim 1$  bar), so the free gas we observe cannot be attributed to boiling of the brine itself. For our pore volume this corresponds to a total amount of dissolved H<sub>2</sub> at near-saturation of

$$n_{\text{sat}} \sim c_{\text{sat}} V_p \approx (1\text{--}3) \times 10^{-8} \text{ mol}, \quad (1)$$

where the range reflects the spread in reported solubilities over the relevant temperature and pressure range rather than uncertainties in our sample geometry.

Batch experiments on olivine and partially serpentinized peridotite at similar temperatures report surface-normalised  $\text{H}_2$  generation rates spanning roughly  $10^{-10}$ – $10^{-8}$   $\text{mol m}^{-2} \text{s}^{-1}$  depending on mineralogy and fluid composition (e.g., Mayhew et al., 2013; Neubeck et al., 2014; McCollom et al., 2016). Complementary flow-through experiments on olivine under hydrothermal conditions indicate comparable order-of-magnitude rates while highlighting the influence of fluid flow and evolving permeability on serpentinization and  $\text{H}_2$  release (Ross et al., 2025). The image-derived grain surface area accessible to the pore fluid within the imaged volume is  $A \approx 4.3 \times 10^{-4} \text{ m}^2$  (Table 1a), so the implied total  $\text{H}_2$  production rate is

$$R \sim rA \sim (4 \times 10^{-14} \text{--} 4 \times 10^{-12}) \text{ mol s}^{-1}. \quad (2)$$

Combining this with the estimate of  $n_{\text{sat}}$  above gives a characteristic time to accumulate near-saturation concentrations of dissolved  $\text{H}_2$  of

$$t_{\text{sat}} \sim \frac{n_{\text{sat}}}{R} \sim 2 \times 10^3 \text{--} 7 \times 10^5 \text{ s}, \quad (3)$$

i.e. roughly 0.5–200 hours when the full range of reported rates is used. If we instead adopt a mid-range literature value of  $r \approx 10^{-9} \text{ mol m}^{-2} \text{ s}^{-1}$ , then  $R \approx 4 \times 10^{-13} \text{ mol s}^{-1}$  and  $t_{\text{sat}} \approx (2\text{--}7) \times 10^4 \text{ s}$ , i.e. approximately 6–20 hours. This narrower range brackets, and is within a factor of a few of, the observed onset time of resolvable bubbles ( $\sim 8$  h). The close agreement between the simple solubility-based timescale and the measured induction period strongly supports an interpretation in which an initial phase of reaction-driven dissolved  $\text{H}_2$  accumulation is followed by gas-phase nucleation, rather than one in which bubbles are produced primarily by instantaneous thermal expansion of pre-existing air or exsolution of background dissolved gases during heating.

Once a critical degree of supersaturation is reached, gas nucleation becomes energetically favourable. Prior to this point, sub-micrometre nuclei may form and redissolve but remain far below the micro-CT resolution (voxel size  $\sim 6 \mu\text{m}$ ). Even when stable bubbles do appear, their total volume can initially be a tiny fraction of the pore volume; for example, a single bubble of diameter  $20 \mu\text{m}$  has a volume of order  $10^{-15} \text{ m}^3$ , corresponding to a gas saturation of  $S_g \sim 10^{-8}$  in the sample. Thus the apparent “no-bubble” regime in the images most likely reflects a combination of real undersaturation and a detection limit: only when the total gas volume exceeds a few tenths of a percent of the pore volume does the gas phase become clearly distinguishable from noise and artefacts in the segmentation.

The rapid increase in gas occupancy between 8 and 23 h, from  $S_g \approx 0.01$  to  $S_g \approx 0.39$  (Table 1b), is consistent with a nucleation-and-growth phase in which many pores cross the supersaturation threshold over a relatively short time interval. In this regime, newly produced  $\text{H}_2$  partitions between further dissolution and growth of existing bubbles.

Assuming a diffusion coefficient for dissolved  $\text{H}_2$  in water of  $D \sim 10^{-9} \text{ m}^2 \text{ s}^{-1}$ , the diffusive length scale over a time  $t$  is

$$\ell_D \sim \sqrt{Dt} \approx 5\text{--}9 \text{ mm} \quad (4)$$

for  $t$  between 8 and 23 h. This is comparable to the characteristic size of the imaged volume, implying that dissolved  $\text{H}_2$  can be redistributed throughout the sample and feed bubble growth over the timespan between scans.

By 23 h, the images show a large, internally connected network of gas ganglia occupying much of the pore space, suggesting that capillary entry pressures have been overcome in a significant fraction of the pore throats and that the system has approached a quasi-steady balance between continued  $\text{H}_2$  generation, dissolution and gas-phase growth.

The more modest changes observed between 23 and 30 h (Fig. 3c,d), during which  $S_g$  increases only slightly from  $\approx 0.39$  to  $\approx 0.43$  and the apparent rate  $\Delta S_g/\Delta t$  drops by almost an order of magnitude (Table 1b), are naturally interpreted as a late-time regime in which (i) the driving force for further  $H_2$  exsolution is reduced as dissolved concentrations approach a new equilibrium with the gas phase, (ii) reactive surface area is locally reduced as alteration rinds and secondary phases develop on grain surfaces, and (iii) additional  $H_2$  produced at depth can diffuse and be taken up by existing bubbles without requiring widespread nucleation of new gas domains. In this view, the observed time sequence reflects a transition from a reaction-controlled build-up of dissolved  $H_2$  (pre-nucleation), through a short nucleation-and-growth episode once supersaturation is reached, to a diffusion- and surface-reaction-limited regime at later times.

Although these back-of-the-envelope calculations are necessarily approximate, they demonstrate that the qualitative evolution seen in the micro-CT time series—now quantified in terms of measured porosity, surface area and gas saturation—is consistent with known  $H_2$  production rates during low-temperature alteration of ultramafic rocks and with simple transport and solubility constraints. More broadly, the results highlight that even in a small, static system, there can be a substantial lag between the onset of water–rock reaction and the formation of a resolvable free gas phase, followed by a relatively short period during which pore-scale connectivity of the gas is established. Such behaviour has important implications for natural  $H_2$  systems: it suggests that zones of intense reaction may remain “invisible” in terms of free gas for extended periods, and that the conditions required to cross nucleation and connectivity thresholds may be highly localised in space and time.

We did not perform a separate brine-only micro-CT control experiment in an inert granular medium, but the early part of our time series effectively provides an internal control: the same apparatus, KI brine and loading conditions show no resolvable gas for the first 8 h, with a gas phase only appearing after prolonged reaction. This behaviour is difficult to reconcile with a purely instrumental or brine-related artefact and instead points to the role of water–rock reaction in driving gas exsolution.

#### 4.1 Implications for natural $H_2$ systems

Although this experiment is deliberately small-scale and exploratory, the observed sequence of (i) delayed bubble appearance, (ii) rapid establishment of a connected gas network, and (iii) later-time, slower growth has several implications for natural  $H_2$  systems and engineered analogues.

First, the long pre-nucleation period implies that substantial water–rock reaction and  $H_2$  production can occur before a free gas phase becomes detectable at the pore scale. In natural settings, zones of active  $H_2$  generation may therefore be dominated by dissolved  $H_2$  for extended periods, with little or no expression as free gas until local supersaturation and favourable nucleation conditions are met. Experimental work on fractured ultramafic rocks likewise shows that serpentinization can rapidly seal existing flow paths by reducing fracture permeability by orders of magnitude, implying that sustained fluid and gas transport requires continual generation of new permeability (Farough et al., 2016). This behaviour is directly relevant to proposals for exploiting rock-based hydrogen resources, including “orange hydrogen” schemes that couple water–rock– $H_2$  generation with carbon mineralisation and storage (Osselin et al., 2022).

Second, once nucleation thresholds are crossed, the rapid transition to a connected gas ganglia suggests that gas connectivity may be established over relatively short timescales compared to the overall reaction history. This is consistent with the view that small changes in capillary entry pressures or wettability can trigger large changes in effective gas mobility (e.g., Thaysen et al., 2023; Jangda et al., 2023; Rezaei et al., 2022). In heterogeneous natural reservoirs, such threshold behaviour is likely to be highly localised, so mi-

gration pathways for natural H<sub>2</sub> may be controlled by a limited number of “activated” reaction zones.

Third, the modest changes between 23 and 30 h highlight that, once a gas phase is established, further H<sub>2</sub> production can be partitioned between dissolution into the surrounding fluid and incremental growth of existing bubbles rather than continued nucleation. This behaviour is directly relevant to both natural H<sub>2</sub> accumulations and underground H<sub>2</sub> storage, where the balance between dissolution, trapping and mobile gas strongly influences storage security and recoverable volumes (Heinemann et al., 2021; Miodic et al., 2023). Our results emphasise that predicting this balance requires not only bulk reaction kinetics, but also an understanding of pore-scale nucleation thresholds and the evolving microstructure of reactive rocks.

Overall, the experiment demonstrates that even in a simple, static system, bubble nucleation and gas connectivity are controlled by the interplay of reaction, transport, and capillary processes. Extending this type of pore-scale, time-resolved imaging to a wider range of mineralogies, p–T conditions and flow regimes will be essential for translating geochemical models of H<sub>2</sub> generation into quantitative predictions of where and when a free H<sub>2</sub> phase can form, migrate and accumulate in the subsurface.

## 5 Conclusions

This proof-of-concept experiment demonstrates that time-resolved 4D micro-CT can be used to monitor the emergence and early evolution of a gas phase generated by water–rock reaction in an ultramafic granular pack at 100°C. Because the results are derived from a single experiment on a crushed granular pack under one set of conditions, they should be viewed as qualitative constraints on pore-scale behaviour rather than quantitative predictions for specific field settings. After an initial period of ~8 hours with no resolvable gas, bubbles nucleate and rapidly form a connected ganglia network, followed by a slower growth phase. Simple order-of-magnitude estimates of H<sub>2</sub> solubility, reaction rates and diffusion lengths show that this three-stage evolution is consistent with delayed supersaturation, threshold-controlled nucleation and subsequent diffusion-limited growth within the imaged volume, and the predicted saturation timescale (6–20 hours) closely matches the observed induction period. This agreement provides strong support for the interpretation that the gas is predominantly reaction-derived H<sub>2</sub> rather than air or steam.

Independent gas measurements and H<sub>2</sub>-indicator strips are consistent with the imaged gas phase being predominantly H<sub>2</sub>, although the experiment was not designed to uniquely determine gas composition or to fully resolve reaction pathways. SEM-BEX observations provide qualitative evidence for localised surface alteration and the development or exposure of secondary phases on grain surfaces, but they do not by themselves demonstrate bulk Al mobilisation or allow unambiguous phase identification. We therefore interpret both the gas and mineralogical observations as qualitative indicators of ongoing fluid–rock reaction and associated gas generation in the sample.

Taken together, the results highlight that a significant amount of low-temperature water–rock reaction can occur before a free gas phase becomes detectable at the pore scale, and that once nucleation thresholds are crossed, gas connectivity can be established over relatively short timescales compared to the overall reaction history. This behaviour has direct implications for natural H<sub>2</sub> systems and underground H<sub>2</sub> storage, where the balance between dissolved, trapped and mobile gas phases controls migration and recoverability. Future work should extend this approach to a broader range of mineralogies, pressures, temperatures and flow regimes, and combine pore-scale imaging with more detailed geochemical and mineralogical characterisation to better quantify the coupling between serpentinization kinetics, gas generation and multiphase transport in reactive ul-

tramafic rocks. The primary contribution of this study is therefore the direct, spatially and temporally resolved observation of gas nucleation and connectivity during low-temperature alteration, rather than detailed identification of the neofomed mineral phases. Future work combining similar imaging with complementary mineralogical and geochemical analyses will be essential to fully resolve the reaction pathways involved.

### Open Research Section

The micro-CT image volumes, processed segmentations, and representative SEM-BEX images used in this study will be made available in an open-access repository (e.g., Zenodo) upon acceptance of the manuscript. A persistent DOI and metadata will be provided in the final published version.

### Conflict of Interest declaration

The authors declare there are no conflicts of interest for this manuscript.

### Acknowledgments

This research was funded by The Carnegie Trust RIG013387. Sample collection was funded by the Gilchrist Educational Trust (grant GILC 06.22, administered by the Royal Geographical Society).

### Author Contributions

H.P.M and A.G. conceptualised this study. H.P.M. raised funding. A.G. chose the sample. M.W. prepared the sample. H.P.M. and Z.Z.J. did the imaging experiment. J.B. did the pre and post experimental SEM-BEX imaging. Z.Z.J. and H.P.M. analysed the micro-CT image data. M.W. analysed the SEM-BEX data. H.P.M. wrote the first draft. All authors contributed to writing this paper.

### References

- Albers, E., Bach, W., Pérez-Gussinyé, M., McCammon, C., & Frederichs, T. (2021). Serpentinization-driven h<sub>2</sub> production from continental break-up to mid-ocean ridge spreading: unexpected high rates at the west iberia margin. *Frontiers in Earth Science*, *9*, 673063.
- Andrew, M., Bijeljic, B., & Blunt, M. J. (2014). Pore-scale imaging of trapped supercritical carbon dioxide in sandstones and carbonates. *International Journal of Greenhouse Gas Control*, *22*, 1–14.
- Boon, M., & Hajibeygi, H. (2022). Experimental characterization of h<sub>2</sub>/water multiphase flow in heterogeneous sandstone rock at the core scale relevant for underground hydrogen storage (uhs). *Scientific reports*, *12*(1), 14604.
- Buades, A., Coll, B., & Morel, J.-M. (2005). A non-local algorithm for image denoising. In *2005 IEEE Computer Society Conference on Computer Vision and Pattern Recognition (CVPR'05)* (Vol. 2, pp. 60–65).
- Bultreys, T., De Boever, W., & Cnudde, V. (2016). Imaging and image-based fluid transport modeling at the pore scale in geological materials: A practical introduction to the current state-of-the-art. *Earth-Science Reviews*, *155*, 93–128.
- Ellison, E. T., Templeton, A. S., Zeigler, S. D., Mayhew, L. E., Kelemen, P. B., Matter, J. M., & Party, O. D. P. S. (2021). Low-temperature hydrogen formation during aqueous alteration of serpentinized peridotite in the samail ophiolite. *Journal of Geophysical Research: Solid Earth*, *126*(6), e2021JB021981.
- Ely, T., Leong, J., Canovas, P., & Shock, E. (2023). Huge variation in h<sub>2</sub> generation

- during seawater alteration of ultramafic rocks. *Geochemistry, Geophysics, Geosystems*, 24(3), e2022GC010658.
- Farough, A., Moore, D. E., Lockner, D. A., & Lowell, R. (2016). Evolution of fracture permeability of ultramafic rocks undergoing serpentinization at hydrothermal conditions: An experimental study. *Geochemistry, Geophysics, Geosystems*, 17(1), 44–55.
- Gaucher, E. C. (2020). New perspectives in the industrial exploration for native hydrogen. *Elements: An International Magazine of Mineralogy, Geochemistry, and Petrology*, 16(1), 8–9.
- Heinemann, N., Alcalde, J., Miocic, J. M., Hangx, S. J., Kallmeyer, J., Ostertag-Henning, C., ... others (2021). Enabling large-scale hydrogen storage in porous media—the scientific challenges. *Energy & Environmental Science*, 14(2), 853–864.
- Holm, N. G., Oze, C., Mousis, O., Waite, J., & Guilbert-Lepoutre, A. (2015). Serpentinization and the formation of h<sub>2</sub> and ch<sub>4</sub> on celestial bodies (planets, moons, comets). *Astrobiology*, 15(7), 587–600.
- Jackson, O., Lawrence, S. R., Hutchinson, I. P., Stocks, A. E., Barnicoat, A. C., & Powney, M. (2024). Natural hydrogen: sources, systems and exploration plays. *Geoenergy*, 2(1), geoenergy2024–002.
- Jangda, Z., Menke, H., Busch, A., Geiger, S., Bultreys, T., Lewis, H., & Singh, K. (2023). Pore-scale visualization of hydrogen storage in a sandstone at subsurface pressure and temperature conditions: Trapping, dissolution and wettability. *Journal of colloid and interface science*, 629, 316–325.
- Jiang, F., & Tsuji, T. (2015). Impact of interfacial tension on residual co<sub>2</sub> clusters in porous sandstone. *Water Resources Research*, 51(3), 1710–1722.
- Lanczos, C. (1956). Applied analysis prentice hall. *New York*.
- Lodhia, B. H., Peeters, L., & Frery, E. (2024). A review of the migration of hydrogen from the planetary to basin scale. *Journal of Geophysical Research: Solid Earth*, 129(6), e2024JB028715.
- Mayhew, L. E., Ellison, E., McCollom, T., Trainor, T., & Templeton, A. (2013). Hydrogen generation from low-temperature water–rock reactions. *Nature Geoscience*, 6(6), 478–484.
- McCollom, T. M., & Bach, W. (2009). Thermodynamic constraints on hydrogen generation during serpentinization of ultramafic rocks. *Geochimica et Cosmochimica Acta*, 73(3), 856–875.
- McCollom, T. M., Klein, F., Robbins, M., Moskowitz, B., Berquó, T. S., Jöns, N., ... Templeton, A. (2016). Temperature trends for reaction rates, hydrogen generation, and partitioning of iron during experimental serpentinization of olivine. *Geochimica et Cosmochimica Acta*, 181, 175–200.
- Menke, H. P., Bijeljic, B., Andrew, M. G., & Blunt, M. J. (2015). Dynamic three-dimensional pore-scale imaging of reaction in a carbonate at reservoir conditions. *Environmental science & technology*, 49(7), 4407–4414.
- Miller, H. M., Matter, J. M., Kelemen, P., Ellison, E. T., Conrad, M. E., Fierer, N., ... Templeton, A. S. (2016). Modern water/rock reactions in oman hyperalkaline peridotite aquifers and implications for microbial habitability. *Geochimica et Cosmochimica Acta*, 179, 217–241.
- Miocic, J., Heinemann, N., Edlmann, K., Scafidi, J., Molaei, F., & Alcalde, J. (2023). Underground hydrogen storage: a review.
- Neubeck, A., Duc, N. T., Hellevang, H., Oze, C., Bastviken, D., Bacsik, Z., & Holm, N. G. (2014). Olivine alteration and h<sub>2</sub> production in carbonate-rich, low temperature aqueous environments. *Planetary and Space Science*, 96, 51–61.
- Noiriel, C., & Renard, F. (2022). Four-dimensional x-ray micro-tomography imaging of dynamic processes in geosciences. *Comptes Rendus. Géoscience*, 354(G2), 255–280.
- Noiriel, C., & Soulaire, C. (2021). Pore-scale imaging and modelling of reactive

- flow in evolving porous media: Tracking the dynamics of the fluid–rock interface. *Transport in porous media*, *140*(1), 181–213.
- Osselin, F., Soullain, C., Fauguerolles, C., Gaucher, E., Scaillet, B., & Pichavant, M. (2022). Orange hydrogen is the new green. *Nature Geoscience*, *15*(10), 765–769.
- Oze, C., & Sharma, M. (2007). Serpentinization and the inorganic synthesis of h<sub>2</sub> in planetary surfaces. *Icarus*, *186*(2), 557–561.
- Prinzhofer, A., & Deville, E. (2015). Natural hydrogen: The new geologic energy frontier. *Oil Gas Sci Technol*, *70*(5), 727–32.
- Rezaei, A., Hassanpouryouzband, A., Molnar, I., Derikvand, Z., Haszeldine, R. S., & Edlmann, K. (2022). Relative permeability of hydrogen and aqueous brines in sandstones and carbonates at reservoir conditions. *Geophysical Research Letters*, *49*(12), e2022GL099433.
- Ross, C., Vega, B., Frouté, L., Kim, T.-W., & Kovscek, A. (2025). Hydrogen generation and serpentinization of olivine under flow conditions. *Geophysical Research Letters*, *52*(6), e2024GL114016.
- Schrenk, M. O., Brazelton, W. J., & Lang, S. Q. (2013). Serpentinization, carbon, and deep life. *Reviews in Mineralogy and Geochemistry*, *75*(1), 575–606.
- Sleep, N., Meibom, A., Fridriksson, T., Coleman, R., & Bird, D. (2004). H<sub>2</sub>-rich fluids from serpentinization: geochemical and biotic implications. *Proceedings of the National Academy of Sciences*, *101*(35), 12818–12823.
- Thaysen, E. M., Butler, I. B., Hassanpouryouzband, A., Freitas, D., Alvarez-Borges, F., Krevor, S., ... Edlmann, K. (2023). Pore-scale imaging of hydrogen displacement and trapping in porous media. *International Journal of Hydrogen Energy*, *48*(8), 3091–3106.
- Wang, J., Watanabe, N., Okamoto, A., Nakamura, K., & Komai, T. (2019). Enhanced hydrogen production with carbon storage by olivine alteration in co<sub>2</sub>-rich hydrothermal environments. *Journal of CO<sub>2</sub> Utilization*, *30*, 205–213.
- Wiesenburg, D. A., & Guinasso Jr, N. L. (1979). Equilibrium solubilities of methane, carbon monoxide, and hydrogen in water and sea water. *Journal of chemical and engineering data*, *24*(4), 356–360.
- Yekta, A., Manceau, J.-C., Gaboreau, S., Pichavant, M., & Audigane, P. (2018). Determination of hydrogen–water relative permeability and capillary pressure in sandstone: application to underground hydrogen injection in sedimentary formations. *Transport in Porous Media*, *122*(2), 333–356.
- Zgonnik, V. (2020). The occurrence and geoscience of natural hydrogen: A comprehensive review. *Earth Science Reviews*, *203*(1), 103140.